

In-operando XRD Study of the Effects of Water Vapor on Phase Formation in LSM/YSZ SOFC Cathodes

X. Yang,^a J. S. Hardy,^{a†} C. A. Coyle,^a J. F. Bonnett,^a S. M. Mahserejian,^a and J. W. Stevenson^a

^a Pacific Northwest National Laboratory, 902 Battelle Blvd, Richland, WA99352, USA

*Corresponding author: john.hardy@pnnl.gov

Abstract

In-operando XRD was conducted on anode supported SOFC button cells with LSM-YSZ cathodes operated at varying cathode air compositions under constant current conditions for over 1000 hours. 1-hour XRD scans were continuously collected throughout the entire operation duration. By taking the sum of measured intensities from all of the collected patterns, the resulting cumulative XRD count times allowed the identification of minor phases present at concentrations as low as <0.1 wt%. In dry air with no contaminants, the cathode exhibited improving power output during the first couple of hundred hours, followed by stable operation. The effect of 3% H₂O + 12% CO₂ on the LSM-YSZ cathode was very similar to the effect of 3% H₂O alone, exhibiting performance degradation. Increasing contaminants in the cathode air were found to decrease the performance of the cells. *In-operando* XRD discovered an increase in MnO concentration and decrease in La₂O₃. A gradual expansion of the LSM lattice resulting from loss of Sr or O was discovered in the LSM/YSZ cathodes tested in humid cathode air. The inverse relationship between the unit cell volume and operating voltage suggests a possible correlation between Sr segregation and performance degradation in the LSM/YSZ cathodes.

Keywords *In-operando* XRD, LSM-YSZ cathode, Sr Segregation, Performance degradation, Impedance spectroscopy

Introduction

Among the most prominent SOFC cathode materials is the $(\text{La}_{0.8}\text{Sr}_{0.2})_{1-x}\text{MnO}_{3-\delta} / \text{Zr}_{0.84}\text{Y}_{0.16}\text{O}_2$ (LSM/YSZ) composite due to its electrocatalytic activity for oxygen reduction, electronic conductivity greater than 200 S cm^{-1} in LSM, and its thermomechanical and chemical compatibility with the adjacent YSZ electrolyte.(1-7) YSZ is often combined with the LSM to form a composite cathode because LSM alone, while having high electronic conductivity, has very low ionic conductivity. This limits the oxygen reduction reactions in LSM cathodes to regions in very near proximity to the triple phase boundary (TPB) which is extended into the cathode layer by adding the YSZ.

While the power density of cells with LSM-based cathodes is generally lower than that of single-phase mixed ionic electronic conducting cathodes such as lanthanum strontium cobalt ferrite (LSCF), the stability in performance is often better. However, even in light of improved stability, degradation mechanisms persist. Morphological changes such as loss of active surface area and TPB length caused by sintering at operating temperatures under current load have been correlated to degradation.(8-12) Thermomechanical stresses can result in delamination between component layers.(13, 14)

Zheng et al.(15) carried out a systematic XRD study of the phase behavior of LSM with varying A/B cation ratios and found that when $A/B < 1$, Mn_3O_4 formed as a secondary phase that they indicated can enhance cathode performance; and when $A/B \geq 1$, La_2O_3 , $\text{La}(\text{OH})_3$, and $(\text{La,Sr})_2\text{MnO}_4$ formed as secondary phases. They pointed out that La_2O_3 and $\text{La}(\text{OH})_3$ are undesirable phases due to their low conductivities and detrimental effects on mechanical strength. These phases also react with YSZ to form highly resistive $\text{La}_2\text{Zr}_2\text{O}_7$.(12, 16, 17) Strontium has been found to segregate to the surface of LSM(18-20) and decrease electron transfer activity in the oxygen

reduction reaction.(21, 22) Segregated Sr may also react with YSZ to form resistive SrZrO₃.(14, 23, 24)

Extrinsic contaminants, most notably Cr, carried to the cathode in the oxidizer gas stream are known to poison the cathode.(14, 25-29) Moisture in the cathode air has also been reported to contribute to degradation through mechanisms including Mn-depletion and LSM decomposition at the LSM/YSZ interface,(30-35) microstructural coarsening,(34) Sr segregation,(35, 36) increased impurities volatilization(33, 37, 38) and segregation to TPB areas,(39, 40) alteration of the surface properties of the cathode,(32, 33, 40) zirconate formation,(35) and general acceleration of the degradation processes that occur in dry air.(40) Liu et al. found that, in humid cathode air, degradation increases as temperature decreases.(31) Carbon dioxide was reported to reduce performance and increase polarization resistance by inhibiting oxygen dissociation and diffusion on LSM,(41) while other reports found it to have negligible impact on degradation.(42) Thermodynamic modeling predicted that CO₂ could cause SrCO₃ formation that would decrease conductivity.(43) During simultaneous exposure to both moisture and CO₂ in the cathode air, LSM/YSZ cathodes degraded due to segregation of Sr on the cathode surface and formation of La₂Zr₂O₇ at the LSM/YSZ interface. The degradation was largely reversible after removing moisture and CO₂ from the cathode air.(44)

More research suggesting that Sr segregation is an issue in LSM has been reported in recent years using different approaches. Acid etching removed elevated Sr and Mn levels from the active sites on the LSM cathode surfaces, which leads to a significant polarization decrease. (45) Scanning tunneling microscopy/spectroscopy (STM/STS) results showed decreased tunneling conductance where Auger electron spectroscopy (AES) found surface Sr enrichment.(46) Sr surface-doped LSM electrodes exhibited significantly decreased performance.(47) EIS and in-situ X-ray

photoelectron spectroscopy (XPS) and secondary ion mass spectrometry (SIMS) showed that surface SrO is detrimental to the oxygen reduction reaction.(48) In-situ synchrotron total reflection X-ray fluorescence (XRF) showed Sr segregation over a wide range of Temperature and pO_2 .(49)

In many tests it has been found that during the initial tens of hours to several weeks, an increase in performance occurs prior to the onset of degradation. This behavior is often referred to as cathode activation, conditioning, or burn-in.(50-53) Several mechanisms for this phenomenon have been put forward, including partial reduction and increased oxygen vacancy concentration leading to improved oxygen ion diffusion;(54-63) microstructural modification and increased TPB length;(64-67) changes in the surface composition of LSM or YSZ in the cathode,(60, 67-70) or dissociation or redissolution of resistive interfacial phases.(71-74)

As evidenced in the preceding discussion, much work has been done to uncover numerous mechanisms that contribute to degradation in LSM/YSZ cathodes. Traulsen et al.(75) discusses the many reasons why in-operando techniques are key to advancing the science of electrochemical solid oxide cells such as SOFCs. While the emphasis of their paper was on surface analysis techniques, the in-operando XRD characterization discussed in the present paper, although not surface sensitive, nonetheless provides additional information to the scientific volume that contributes to a more complete understanding of what occurs in the LSM/YSZ cathode during operation of anode-supported cells.

Experimental

Cell Preparation

Anode-supported electrolyte substrates were fabricated through a non-aqueous tape-casting and lamination process. For the bulk anode, 1.3 grams of NiO [J.T. Baker, Avantor Performance

Materials, Center Valley, PA] per gram of 5YSZ [Imery's Fused Minerals, Laufenburg, Germany] were attrition milled together in isopropanol with 3 mm spherical zirconia milling media. The resulting slurry was then dried overnight in a stainless steel pan on a drying radiator at 90°C, leaving a powder mixture that was added to a mixture of methyl ethyl ketone (MEK), ethanol, PS131 dispersant [Akzo Nobel, Pasadena, TX], and Cancarb N990 carbon black [Cancarb Ltd., Medicine Hat, Alberta, Canada] and ball milled in a Nalgene container with barrel-shaped zirconia milling media. After 4 hours of ball milling, Butvar B-79 [Solutia, San Ramon, CA] and benzyl butyl phthalate [Fisher Scientific, Waltham, MA] were added to the slurry for at least 10 hours of milling at 30 rpm followed by another 2 hours at 6 rpm. The slurry was tape cast at a green thickness of ~125 μm on silicon coated Mylar.

For the active anode, 1.89 grams of NiO per gram of 8YSZ [Daiichi Kiegenso Kagaku Kogyo Co. Ltd., Japan] were attrition milled in isopropanol and dried. The resulting powder was ball milled in MEK, ethanol, and dispersant for at least 4 hours at 60 RPM before Ethocel 45 [Dow Chemical, Midland, MI] and dibutyl phthalate [Fisher Scientific, Waltham, MA] were added and ball milling continued overnight. The slurry was then tape cast onto glass with a green thickness of 15 μm .

The electrolyte was batched using the same 8YSZ powder as the active anode but without attrition milling before ball milling. A slurry with a solids loading of 16.7 vol% was ball milled and tape cast in same manner as described for the active anode.

The bulk anode tape was cut to the desired length and placed on the silicon-coated side of Mylar with the cast side facing down toward the Mylar and the air side facing up. Eleven pieces of bulk anode were stacked upon one another, with each piece rotated 180° relative to the previous piece in order to even out any thickness differences that may exist across

the width of the tape. One layer of active anode tape was then placed on top of the stack of bulk anode tapes with the cast side facing up and the air side facing down toward the bulk anode tapes. One layer of electrolyte tape was then placed on top of the active anode with the cast side down. The uncoated side of a sheet of Mylar was placed on top of the electrolyte and the assembly was vacuum sealed in a vacuum bag. The sealed vacuum bag was fed into a 135°C roll laminator four times, rotating the vacuum bag 90° each time. The laminator pressure was 20 psi on the first pass, 30 psi on the second pass, and 40 psi for the last two passes. Circular pieces were laser cut from the resulting laminate and sintered at 1385°C for 2 hours in air. The pieces were then creep flattened at 1350°C for 2 hours in air. After sintering, the substrates were approximately 13 mm in diameter and 1 mm thick. A Ni mesh was then embedded into NiO paste on the anode side of the substrate to serve as the anode current collector. The anode current collector was sintered at 1200°C for 2 hours in air. LSM-YSZ cathode powder [Fuel Cell Materials, Lewis Center, OH] with the nominal chemical formula $(\text{La}_{0.8}\text{Sr}_{0.2})_{0.95}\text{MnO}_{3-\delta} - (\text{Y}_2\text{O}_3)_{0.08}(\text{ZrO}_2)_{0.92}$ that had been attrition milled for 5-10 hours until the average particle size was approximately 0.35 μm was mixed into V-006 binder at a solids loading of 40 wt%. The resulting ink was applied to the anode-supported electrolyte by screen printing. Four prints were applied using a commercial screen [Sefar, Buffalo, NY] with 230 mesh, 1.1 mil wire, and 1 mil emulsion thickness and subsequently sintered at 1200°C.

After sintering, the circular cathode had an area of 0.5 cm^2 . In order to avoid shielding the cathode from impinging x-rays during diffraction measurements, a gold paste current collector was applied only to the perimeter of the cathode and contacted by a matching ring of gold mesh, leaving the center of the cathode uncovered. The cell was placed in a furnace

to fire the current collector at 875°C for 2 hours in air. A sealing glass developed at PNNL (designated G-18) was used to seal the cells to the alumina test fixture which was designed to allow small-scale button cells to be operated in the high temperature x-ray diffractometer (HTXRD) while diffraction spectra are simultaneously being collected from the working cathode.⁽⁷⁶⁾ The top of the test fixture with a button cell attached is shown in Figure 1. The test fixture was inserted into the HTK 1200 heating chamber [Anton Paar, Ashland, VA] of the D8 Advance XRD [Bruker AXS, Madison, WI] as shown in Figure 2. The cell was heated to 830°C for 1 h for glass sealing and then cooled to the designated operating temperature. Nitrogen at a flow rate of 75 sccm was used to purge the anode side of the fixture for about an hour. Hydrogen with 3% water vapor was then introduced at a flow rate of 75 sccm to the anode which was allowed to undergo reduction before the intended operating voltage was applied to the cell. Upon reduction, the composition of the functional anode layer was 50 vol% Ni and 50 vol% 8YSZ and the bulk anode layer was 40 vol% Ni and 60 vol% 5YSZ. Air with a dew point of less than -40°C was used as the oxidant gas. For tests with carbon dioxide added to the cathode air, carbon dioxide was mixed into the cathode air stream at a concentration of 12% as measured by a mass flow controller. From our experience, the CO₂ concentration may reach as high as 6% in some cases by recirculation of the cathode air. Therefore, to exaggerate any effect of CO₂, 12% of CO₂ was added to the cathode air stream, doubling the maximum expected concentration. For tests with water in the cathode air, the air with or without added carbon dioxide was bubbled through deionized water to saturate it with ~3% moisture and subsequently directed at the cathode surface at 350 sccm through a fused silica tube.

One of the industry partners we were working with recirculated their cathode air and believed that the CO₂ concentration may have reached as high as 6% in some cases. Therefore, to exaggerate any effect of CO₂, we decided to test at 12%, doubling the maximum expected concentration

Electrochemical Testing

The LSM-YSZ cathodes were tested at 775°C and constant current at ~0.8 V in air containing no additional contaminants or containing ~3% water with or without 12% carbon dioxide. The current-voltage and electrochemical impedance spectroscopy (EIS) data were recorded using a Solartron 1480 Multistat and 1255 Frequency Response Analyzer [AMETEK Advanced Measurement Technology, Farnborough, Hampshire, UK]. For cells tested at ~0.8 V, performance data was recorded at the current that was measured when cell operation was initiated at an operating voltage of 0.8 V. During intermittent EIS measurements, the cell was subjected to a dc operating voltage of 0.8 V with an ac amplitude of 20 mA.

XRD Data Collection and Analysis

During the entire duration of cell testing, XRD scans covering 25 to 85° 2θ with 0.02° steps and a 1.1 second count time per step were initiated every hour. The XRD instrument was outfitted with a Cu Kα1 radiation source, a Göbel mirror, a 0.12° diffracted beam Soller slit, and a Sol-X energy dispersive x-ray detector [Bruker AXS] that filters out Kβ peaks and fluorescence background. The resulting series of XRD patterns was divided into subseries of equal numbers of patterns that were integrated to form a series of summation patterns by taking the sum of the measured intensities at each diffraction angle. These integrated XRD patterns facilitated finding time-dependent changes in the cathode in two

ways. First, the count statistics and signal-to-noise ratios were greatly improved as compared to the individual 1 hour patterns, and second, the longer effective time between patterns allowed the gradual changes more time to progress and therefore to be more easily resolved than the small change that might happen over a single hour. Because of the very gradual and subtle nature of the changes in the XRD patterns, a single XRD pattern created by integrating all of the XRD patterns collected over the entire duration of each cell test was used for phase identification and to determine the average composition of the cathode over the course of the test. The count statistics resulting from the integration of several hundred hours of XRD scans allow phases present in concentrations of less than 0.1 wt% to be identified.

Jade [v9.6.0, Materials Data, Inc., Livermore, CA] software was employed for XRD analysis. The 'Merge Overlays' function of Jade was used for pattern integration. The 'Search/Match' function was used to identify phases from the PDF-4+ 2018 database [International Centre for Diffraction Data, Newtown Square, PA]. 'Peak Painting' was used to determine the area under the major peaks for estimation of the phase concentrations using the reference intensity ratio (RIR) method.

Jade's Rietveld refinement algorithm that they refer to as 'Whole Pattern Fitting (WPF) Refinement' was used for determining lattice parameters of phases in the cathode. The refinement covered the entire pattern from 25-85° 2θ while using the Cu Kα₁ wavelength of 1.54059Å to compute d-spacings. The Kα₂ peaks were not stripped prior to refinement and peak centroids were assumed to represent the peak location. The background intensity was fit using a parabolic curve

and a pseudo-Voigt profile shape function was used to fit the peaks. Global fitting parameters included specimen displacement (SD) and $K\alpha_2/K\alpha_1$ intensity ratio. Phase-specific fitting parameters included lattice parameters and temperature factors (TF).

Statistical analysis

The HT-XRD patterns were carefully inspected at a variety of times and integration sizes. The smallest integration size at which a change between patterns could be distinguished was used to characterize the phase evolution. The phase peaks were integrated by different consecutive period of time: 250 h, 500 h, 750 h and 1100 h in dry air; 350 h, 700 h and 1050 h in humid air; 337 h, 674 h and 101 h in humid air with 12% CO₂. The *d*-spacing values corresponding to a group of reflection peaks of each phase were obtained by multiple-phase Rietveld refinement using the integrated HT-XRD patterns. The hypothesis for dry experiment is that LSM and YSZ are the shifting phases and Al₂O₃ is the stationary phase. For the experiment in humid air with and without added CO₂, the LSM phase was assumed to be shifting while the YSZ and Al₂O₃ phases were assumed to be stationary.

Statistical methods

In order to analyze the stationary/shifting properties of phases, data representing changes in peak centroid positions throughout the experiments are first needed. To quantify the peak shifts, three variables were calculated using the raw *d*-spacing results obtained by Rietveld Refinement. First, time separated relative shifts (i.e. time dependent % change) were obtained by calculating the percent shift in peak position between every pair of consecutive time steps. Note that number of shifts measured for each peak equals to 1 less than the number of time measurements for each peak, which creates a set of shift values for each pair of consecutive times (see boxplots with time labeled relative shifts in Figure 11). This

first dataset provides the most detail about how peaks shift during each possible time period. Second, time independent relative shifts were obtained by consolidating all of the time separated relative shifts for each phase group, such that the corresponding time periods are not considered, which creates a single set of shift values for each experiment (see “All Times” labeled boxplots in Figure 11). This second dataset is most useful when assuming that peak shifts are consistent throughout an experiment duration. Third, time dependent slopes were obtained by linear regression fits for each peak and its positions sampled through all points in time, which creates a single set of slope values for each experiment (see “Slopes” labeled box plots in Figure 11). This third dataset best represents the overall shifting trend of each peak throughout the entire experiment by considering detailed information provided at each time point, while also providing only a single value to represent the general shifting behavior. Data from these three datasets were used to study the shifting properties of each phase group, as well as their relationship to each other.

Shifting and stationary properties of the different phase groups were assessed using hypothesis testing via the Wilcoxon-Mann-Whitney non-parametric U-tests which are appropriate for their use with relatively small datasets, where the specific distribution function of the data is unknown, yet a comparison of the mean values of the tested groups can still be made.⁽⁷⁷⁻⁷⁸⁾ In practice, a hypothesis test is used to make a comparison through a p -value, probability of the null hypothesis being true, which is then compared to α , a significance level used to reject the null hypothesis if the p -value $< \alpha$. Failing to reject the null hypothesis implies that there is a lack of evidence to show that the null hypothesis is not true.

More specifically, three tests were used to analyse the shifting properties of each group, as well as compare the phase groups to each other. Test 1 compared the means of each group to a zero value, which effectively tested if the phase group was stationary in an absolute sense. The hypotheses for Test 1 were defined as $H_0^1: \mu_X = 0$ and $H_a^1: \mu_X \neq 0$, where H_0^1 is the null hypothesis, H_a^1 is the alternative hypothesis, and μ_X is the mean of phase group X. If the corresponding p -value $< \alpha$, then there would be enough evidence to reject the null hypothesis, H_0^1 , and therefore accept that H_a^1 is true (i.e. that group X is not stationary). Test 2 compared the phase groups to each other, which tests if any two groups compared could come from a distribution with the same mean. The hypotheses for Test 2 were defined as $H_0^2: \mu_X = \mu_Y$ and $H_a^2: \mu_X \neq \mu_Y$, where H_0^2 is the null hypothesis, H_a^2 is the alternative hypothesis, and μ_X and μ_Y are the means of phase groups X and Y respectively. If the corresponding p -value $< \alpha$, then there would be enough evidence to reject the null hypothesis, H_0^2 , and therefore accept that H_a^2 is true (i.e. that group X and group Y do not come from the same distributions). The hypotheses for Test 3 were defined as $H_0^3: \mu_X \leq \mu_Y$ and $H_a^3: \mu_X > \mu_Y$, where H_0^3 is the null hypothesis, H_a^3 is the alternative hypothesis, and μ_X and μ_Y are the means of phase groups X and Y respectively. If the corresponding p -value $< \alpha/2$, then there would be enough evidence to reject the null hypothesis, H_0^3 , and therefore accept that H_a^3 is true (i.e. that group X has shifts more in the positive direction than group Y). For all tests, the significance level was set as $\alpha = 0.05$, which indicates a 5% risk of concluding that a difference exists when no actual difference exists. All three tests were conducted for comparing the phase groups using the three variables representing the different quantities for peak shifts. Though a more complete and nearly exhaustive set

of tests were conducted, the relevant results for the experiments in this study are displayed in Table 3.

Results

Electrochemical Testing

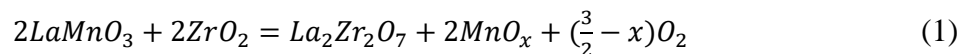
The power densities of the cells with LSM-YSZ cathodes that were tested for over 1000 hours in the *in-operando* XRD test stand are plotted in Figure 3. In this figure and others throughout the remainder of this manuscript, the cell with the cathode tested in clean, dry, uncontaminated air is represented in red; the one tested in air with 3% water added is represented in blue; and the cell tested in air containing 3% water and 12% carbon dioxide is represented in green. Increasing levels of contaminants in the cathode air were found to decrease the performance of the cells. The cell with no added water or carbon dioxide generated more than 0.3 Wcm^{-2} , while the cell with only moisture added to the air generated between $0.2 - 0.25 \text{ Wcm}^{-2}$, and the cell with both moisture and carbon dioxide in the air only generated about 0.15 Wcm^{-2} . Contaminated air also caused degradation in performance while the cell with clean dry air demonstrated an initial increase in performance followed by stable operation.

The results of impedance spectroscopy are summarized based on analyzing the real axis intercepts of each of the collected spectra to determine the ohmic and polarization contributions to the total area specific resistance (ASR) in Figure 4. As expected, the trends in power density (see Figure 3) are reflected in total ASR. Cells with higher total ASR exhibited lower power density and the two cells exposed to contaminated cathode air that exhibit increasing ASR as a function of time undergo time-dependent degradation in performance. Polarization resistance appears to be the dominant contributor to the total ASR and to play a key role in performance stability.

X-ray Diffractometry

Phase Identification. An integrated XRD pattern created by taking the sum of all patterns from the LSM-YSZ cathode over the course of the entire test performed in clean dry cathode air at 775 °C under constant current is shown in Figure 5. The intensity of all peaks is amplified to facilitate examining minor phases. This XRD pattern contained detectable amounts of each of the phases identified in the cathodes operated under any cathode air compositions investigated in this study and it indicates that hundreds of hours of cumulative count time makes it possible to identify even minute concentrations of secondary phases. All identified peaks in Figure 5 are labeled with numbers that correspond to phases formed from the LSM-YSZ cathode and letters that correspond to phases from sources extrinsic to the cathode. Note that peaks are labeled with phases that have predominant contributions to each reflection peak since many phases have several overlapping peaks with other phases.

Since gold mesh and Pt wires were used for cell assembly, gold and platinum phases were observed in the *in-operando* XRD test. The alumina phase results from the alumina test fixture inserted into the HTK 1200 heating chamber of the XRD instrument. The secondary phases contained in the LSM-YSZ cathode after over 1000 hours of operation in dry air can be indexed to Mn_3O_4 , MnO , La_2O_3 , and $La_2Zr_2O_7$, which is comparable to previous literature reports.(79-81) The LSM reacts with YSZ preferentially to form MnO_x and $La_2Zr_2O_7$ (82):

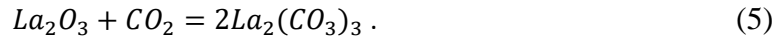
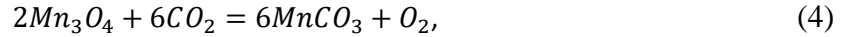


The presence of La_2O_3 phase can be associated with LSM decomposition that can occur at high sintering temperature.(82) No $\text{SrO}/\text{Sr}(\text{OH})_2$ was detected in the cathode tested in any cathode air compositions investigated in this study. Two minor peaks at $2\theta = 26^\circ$ and 42° remained unidentified in this integrated XRD pattern.

To investigate the correlation between the phase composition and the performance degradation, Rietveld refinement was performed using the integrated XRD dataset over the entire test duration in various cathode air compositions under constant current. Table 1 lists the average composition of the LSM-YSZ cathodes tested in air containing no additional contaminants or containing ~3% water with or without 12% carbon dioxide. The cathodes consisted of 43 - 47.5 wt% LSM, 42.1 - 47.5 wt% YSZ and 0.3 - 1.9 wt% tetragonal YSZ in all cases. The concentration of the secondary phases for the cathode operated in air with 3% water was found to be close to that operated in dry air including 1.7 -3.2 wt% of Mn_3O_4 , 1.0 - 2.3 wt% of MnO and 1.8 - 2.1 wt% of La_2O_3 . The $\text{La}_2\text{Zr}_2\text{O}_7$ contained in the cathodes were found to be ≤ 0.1 wt%. The effect of 3% $\text{H}_2\text{O} + 12\%$ CO_2 on LSM-YSZ was very similar to the effect of 3% H_2O alone except increased MnO and decreased La_2O_3 . The MnO detected in the cathode tested in air with 3% $\text{H}_2\text{O} + 12\%$ CO_2 was up to 6.0 ± 0.9 wt%, while the concentration of La_2O_3 dropped to 0.3 ± 0.1 wt%.

The difference in the initial power output is mostly related to the oxygen partial pressures of the different testing environments as shown in Figure 5. The LSM-YSZ cathode operated in clean dry air demonstrated a stable operation after the initial conditioning, while the cathode operated in air with contaminations (3% H_2O with or without 12% CO_2) exhibited gradual performance degradation over time. Even though no carbonates were detected by *in-operando* XRD of the

cathode, a difference in the secondary phases was observed when the cathode air contained water and/or carbon dioxide contaminants. The chemical reactions may include



As the free energy for carbonate formation decreases with operating temperature, no carbonate phases were detected by in-operando XRD in the LSM-YSZ cathode operated at 770 °C. In the LSM-YSZ cathode tested in air with 3% water and 12% carbon dioxide, an increase in MnO concentration and decrease in La₂O₃ were the main changes in phase composition compared with that operated in air with or without water vapor. When the cathode air contains 3% water vapor and 12% carbon dioxide, an increase in MnO suggests that the presence of water vapor suppresses the reaction between manganese oxide and carbon dioxide to form carbonates. A decrease in La₂O₃ concentration suggests that the presence of water vapor and carbon dioxide promotes the reaction between La₂O₃ and YSZ to form La₂Zr₂O₇, corresponding to a slight increase in the La₂Zr₂O₇ concentration. Since the difference in phase composition in the cathode operated in dry air and moist air is small, the reason behind the performance degradation could be also related to other factors.

Visual Inspection and Comparison of Peaks. The *in-operando* XRD measurements provided an insight into gradual changes occurring in the cathode over the entire operation duration. Visual inspection and comparison of series of integrated XRD patterns tested under each condition were performed. Figure 6 shows the phase evolution of the LSM-YSZ cathode operated in clean dry air at 775 °C at ~0.8 V. Summation of every 250 individual *in-operando* XRD patterns were used to investigate gradual changes at the atomic structural level. As shown in Figure 6, no new phases were generated and minor peak shifts were observed but difficult to distinguish without close inspection. Gradual peak shifts were detected for at least one phase in each cell test, and all peaks associated with the affected phases exhibited the observed shift. Thus, only a few representative peaks were selected to illustrate the observed trends. Figure 7 demonstrates the gradual peak shifts of LSM using series of integrated *in-operando* XRD patterns from tests performed with the varying cathode air compositions. A gradual shift of the peaks associated with LSM toward higher angles was observed for the LSM-YSZ cathode tested in clean dry air, while the two cathodes in humid air with or without added CO₂ exhibited a gradual shift of the major peaks of LSM toward lower angles. That is, a lattice contraction occurred very gradually over the 1000 hours of operation in dry air and a lattice expansion occurred in LSM in humid testing conditions.

The peak shifts of YSZ in the series of integrated *in-operando* XRD patterns during tests performed at ~0.8V under various cathode air compositions is shown in Figure 8. A gradual shift of the peaks associated with YSZ toward higher angles was observed for the LSM-YSZ cathode tested in clean dry air, indicating that a slight unit cell lattice contraction occurred during the test. No systematic peak shift was observed for YSZ in the other two cathodes tested in humid air.

Unit Cell Volume. Rietveld refinement was conducted with the integrated *in-operando* XRD patterns operated at different cathode air compositions to discover the changes in unit cell volume of LSM tested at various cathode air compositions at ~0.8V, (see Figure 9). The initial unit cell volumes of LSM in dry air, humid air and humid air with added carbon dioxide were calculated to be 360.54 Å, 360.71 Å and 360.18 Å, respectively. The cell tested in dry air exhibited LSM contraction at a rate that decreases over time. While both cells in humid air exhibited LSM expansion at similar rate. The contraction rate of the unit cell volume of LSM in dry air was calculated to be 0.04% over ~600 hours of operation. The expansion rate of the LSM unit cell in humid air was 0.11% (3% H₂O) and 0.08% (3% H₂O + 12% CO₂), respectively. Possible causes of LSM lattice expansion include but are not limited to loss of Sr and O.(83-85) The rate of Sr loss correlating to the expansion rate of LSM unit cell lattice is listed in Table 2.

Potential Correlation to Degradation. To provide additional insight into the reasons leading to performance degradation, the operating voltage of each cell was recorded during the entire operation at constant current, as shown in Figure 9. The cathode operated in dry air showed an initial increase in operation voltage, followed by relatively stable operation, while the cathodes operated in humid air with or without added carbon dioxide showed a significant degradation over time. The slight decrease in the operating voltage of the cell with the LSM-YSZ cathode operated in clean dry air may result from the microstructural change in the H₂ electrode, which is mainly caused by coarsening of Ni. The microstructural change in the anode occurred in all cathode air compositions studied. Thus, the coarsening of Ni likely accounts for the slight decrease in operating voltage when operated in clean dry air. While Sr segregation explains the significant degradation when operated in contaminated cathode air.(86) As Sr segregation leads to strain in the LSM lattice, the

inverse unit cell volume of LSM evaluated by in-operando XRD refinement were also included in Figure 9. The results indicate an inverse relationship between the unit cell volume of LSM and operating voltage (power density) for all cathodes tested in this study, which provides another piece of experimental evidence suggesting that Sr segregation may promote performance degradation of the LSM cathode.

Statistical Evaluation of Peak Shifts. As suggested by visual inspection of the XRD patterns at a variety of times and integration sizes, the HT-XRD peaks appeared to shift toward a higher or lower 2θ range for the LSM and YSZ phases in different cathode air compositions. Meanwhile, the HT-XRD peaks for several phase compositions exhibited time-independent behavior, including the platinum, gold and alumina. The relative changes in d -spacing associated with centroid peak positions were determined using Rietveld refinement. Changes (or shifts) in peak positions were calculated using the three variables described in the “Statistical methods” section. To analyze the stationary or shifting properties of each group of peaks for each composite, the three versions of hypothesis testing via Wilcoxon-Mann-Whitney non-parametric U-test was performed as described in the “Statistical methods” section. The actual computation of the p -values for Tests 1, 2, and 3 utilized the “`wilcox.test()`” function from the “stats” package in the R programming language.⁽⁸⁷⁾ Table 3 summarizes the p -values with respect to each hypothesis test using different quantities for peak position movements (time separated % shift, all time % shift and slopes). The distribution of values with respect to the statistical significance of the peak shifts are given in boxplots in Figure 11, which provide a visual representation of the hypotheses that the p -values confirmed. In the dry experiment, alumina was selected as the internal standards and was used to represent the non-shifting phase to estimate the statistical significance of the peak shifts for the LSM and YSZ phases. In the humid experiment with and without added CO_2 , alumina and YSZ were assumed as

stationary phases with LSM as shifting phase. The Al_2O_3 peaks were anticipated to be stationary and inert to different experimental conditions. Thus, any observed shifts would be a result of equipment or measurement methods used, i.e. systematic effects of the measurement process.

In the dry experiment, Test 1 for Al_2O_3 peak shifts indicated that they are indistinguishable from zero, verifying the alumina phase to be stationary. Test 1 for LSM and YSZ peak shifts indicated that they are different from zero, confirming they are shifting phases. An exception occurred from 500 h - 750 h, where the boxplot in Figure 11(a) displays that LSM peak shifts are centered around zero from 500 h- 750 h of operation. Test 1 failed to reject that LSM peaks during this period have a mean equivalent to zero, and Test 2 failed to reject that the mean of LSM peaks were different than the means of stationary alumina peaks; however a rather wide distribution of LSM peak movement in clean dry cathode air disproves that these peaks were stationary (see boxplot in Figure 11(a), where the LSM peak shifts are larger in magnitude compared to the stationary alumina peaks). This indicates that the LSM peaks measured between 500 h and 750 h certainly shift, but overall they average out to zero. This inconsistency with the rest of the data from this same experiment could be attributed to noise or errors in measurements. Test 3 provided insight to the ordering of peak shifts, such that LSM peaks shift more to the left than those of YSZ, which shift more to the left than those of the stationary Al_2O_3 phase.

In humid cathode air, Test 1 for LSM peak shifts indicated that they are different from zero, i.e., LSM peaks are confirmed shifting. Test 1 for Al_2O_3 peaks indicated that they are clearly stationary. Test 2 and Test 3 showed that LSM peak shifts are consistently different and larger than YSZ and Al_2O_3 peaks. However, it could not be verified that the YSZ peaks are strictly stationary. YSZ peak shifts are strictly positive between 350 h – 700 h but mostly negative between 700 h – 1050 h. When treating time ranges separately, each set of the strictly positive/mostly negative groups

are more clearly not centered around zero (Test 1 rejected that mean time separated YSZ peak shifts were equivalent to zero); this was also true for the slope values. However, when treating all time ranges together, YSZ peak shifts values are centered around zero, because the positive and negative values balance each other out (Test 1 failed to reject that the mean time independent YSZ peak shifts are equivalent to zero). Similarly, Test 2 rejected that the mean of YSZ peak shifts are the same as the mean of Al_2O_3 peaks when making comparisons using the time-separated measurements, but failed to reject that YSZ peak shifts are indistinguishable from Al_2O_3 peaks when considering the time-independent shifts. This made it difficult to verify that YSZ peak shifts were truly stationary or that they are identical to the Al_2O_3 peak shifts during the humid cathode air experiment.

In the experiments using humid cathode air with added CO_2 , Test 1 rejected that the LSM peak shifts are stationary, Test 2 rejected that mean LSM peak shifts were equivalent to the other phases, and Test 3 confirmed that LSM peak shifts were larger than the other phases. Thus, we can state that LSM peak shifts are indeed shifting, with peaks shifting to larger d -spacing direction. Similarly, Test 1 verified that Al_2O_3 peaks are indistinguishable from zero. However, the YSZ peaks could not be verified as strictly stationary. An exception for the LSM shifts was from the 674 h to 1011 h period, which are considerably less than the shifts during the previous period between 337 h to 674 h; though still positive, the peaks from the 674 h to 1011 h period overlapped significantly with the YSZ and Al_2O_3 peak shifts, thus making it hard to claim that they were indeed shifting in that later period of the experiment (Test 2 comparing LSM to YSZ peak shifts failed to reject that they are equivalent, and Test 3 failed to reject that LSM peak shifts were less than YSZ peak shifts). The hypothesis tests only partially verified that YSZ peaks are close to stationary, since only about half of the slopes and shift comparisons had results favorable to mean

YSZ peak shifts to be centered around zero or to be equivalent to the alumina peak shifts. Furthermore, YSZ peaks had a bias to shift to slightly higher d -spacing directions compared to being absolutely stationary. The slopes and relative shifts independent of time shows that YSZ peak shifts are greater than Al_2O_3 peaks, while the shifts separated by their respective time periods show that YSZ peak shifts are equivalent to Al_2O_3 peaks. Again, this made it difficult to verify that YSZ peak shifts were truly stationary or that they are identical to the Al_2O_3 peak shifts during the humid cathode air with added CO_2 experiment.

Despite having difficulty to verify that YSZ peaks were stationary in the absolute sense, or that their shifts were equivalent alumina peak shifts, YSZ peaks in almost every case were shown shift values smaller in magnitude when compared to LSM peaks. Additionally, qualitative comparisons yield YSZ shifts to be orders of magnitude smaller than LSM shifts, when LSM peaks were determined to be shifted with certainty. Therefore, the lack of evidence for YSZ peaks to be stationary doesn't have to be taken as them being shifting, certainly not like LSM peaks shift.

Scanning Electron Microscopy (SEM). Phase change and lattice expansion during over 1000 hours of operation at constant current at varying cathode air compositions have been confirmed to lead to performance degradation. The surface morphology of a cathode can be considered another factor to affect the long-term stability of a SOFC. Field emission SEM analysis of fracture surfaces of the LSM-YSZ cathodes exposed to various cathode air compositions is displayed in Figure 12. No significant microstructural or chemical differences were found based on the post-mortem SEM images upon exposure to different cathode air compositions.

Summary

In-operando XRD was conducted on fuel cells with LSM-YSZ cathodes operated for over 1000 hours at varying cathode air compositions. The cathode tested in dry air exhibited improved power output, followed by stable operation. Meanwhile the cathode tested in humid air exhibited decreased power density, especially in humid air with added carbon dioxide. The effect of 3% H₂O + 12% CO₂ on the LSM-YSZ cathode was very similar to the effect of 3% H₂O alone. The only observed differences were decreased power density and increased MnO and decreased La₂O₃ detected in the cathode tested in 3% H₂O + 12% CO₂.

Rietveld refinement on a series of *in-operando* XRD suggested that a gradual expansion of the LSM lattice occurred during cell operation in humid cathode air. Loss of Sr or O is known to cause lattice expansion in LSM. An inverse relationship existed between unit cell volume and operating voltage (power density), suggesting a possible correlation between Sr segregation and performance degradation in LSM-YSZ cathodes. Statistical analysis with respect to The relative changes in *d*-spacing associated with centroid peak positions further confirmed the trends of individual peak shifts. Post-mortem SEM observed no significant microstructural or chemical differences on the fracture surfaces of the LSM-YSZ cathodes after exposure to different cathode air compositions during the tests.

Conflicts of interest

There are no conflicts to declare.

Acknowledgements

This work was supported by the Department of Energy Office of Fossil Energy's SOFC program under Contract No. DE-FE66841. The authors would like to thank Shailesh Vora, Patcharin Burke, Debalina Dasgupta, Joe Stoffa and Briggs White from National Energy Technology Laboratory for providing helpful guidance and discussions. Pacific Northwest National Laboratory is operated by Battelle Memorial Institute for the US Department of Energy.

References

1. F. H. vanHeuveln and H. J. M. Bouwmeester, *Journal of the Electrochemical Society*, **144**, 134 (1997).
2. X. J. Chen, S. H. Chan and K. A. Khor, *Electrochem. Solid State Lett.*, **7**, A144 (2004).
3. E. Siebert, A. Hammouche and M. Kleitz, *Electrochim. Acta*, **40**, 1741 (1995).
4. X. J. Chen, S. H. Chan and K. A. Khor, *Solid State Ionics*, **164**, 17 (2003).
5. J. Mizusaki, Y. Yonemura, H. Kamata, K. Ohyama, N. Mori, H. Takai, H. Tagawa, M. Dokiya, K. Naraya, T. Sasamoto, H. Inaba and T. Hashimoto, *Solid State Ionics*, **132**, 167 (2000).
6. A. Hammouche, E. Siebert and A. Hammou, *Mater. Res. Bull.*, **24**, 367 (1989).
7. S. P. Jiang, *J. Mater. Sci.*, **43**, 6799 (2008).
8. M. Kuznecov, P. Otschik, P. Obenaus, K. Eichler and W. Schaffrath, *Solid State Ionics*, **157**, 371 (2003).
9. J. H. Choi, J. H. Jang, J. H. Ryu and S. M. Oh, *Journal of Power Sources*, **87**, 92 (2000).
10. M. J. Jørgensen, P. Holtappels and C. C. Appel, *Journal of Applied Electrochemistry*, **30**, 411 (2000).
11. T. Matsui, Y. Mikami, H. Muroyama and K. Eguchi, *Journal of Power Sources*, **242**, 790 (2013).
12. Y. L. Liu, A. Hagen, R. Barfod, M. Chen, H. J. Wang, F. W. Poulsen and P. V. Hendriksen, *Solid State Ionics*, **180**, 1298 (2009).
13. Y. C. Hsiao and J. R. Selman, *Solid State Ionics*, **98**, 33 (1997).
14. Y. Chen, L. Yang, F. Ren and K. An, *Sci. Rep.*, **4**, 5179 (2014).
15. F. Zheng and L. R. Pederson, *J. Electrochem. Soc.*, **146**, 2810 (1999).
16. S. P. Jiang, J. G. Love, J. P. Zhang, M. Hoang, Y. Ramprakash, A. E. Hughes and S. P. S. Badwal, *Solid State Ionics*, **121**, 1 (1999).
17. H. Y. Lee and S. M. Oh, *Solid State Ionics*, **90**, 133 (1996).
18. N. Caillol, M. Pijolat and E. Siebert, *Appl. Surf. Sci.*, **253**, 4641 (2007).
19. W. Lee, J. W. Han, Y. Chen, Z. H. Cai and B. Yildiz, *J. Am. Chem. Soc.*, **135**, 7909 (2013).
20. T. T. Fister, D. D. Fong, J. A. Eastman, P. M. Baldo, M. J. Highland, P. H. Fuoss, K. R. Balasubramaniam, J. C. Meador and P. A. Salvador, *Appl. Phys. Lett.*, **93**, 3 (2008).
21. K. Katsiev, B. Yildiz, K. Balasubramaniam and P. A. Salvador, *Appl. Phys. Lett.*, **95**, 3 (2009).
22. W. Lee, J. W. Han, Y. Chen, Z. Cai and B. Yildiz, *J. Am. Chem. Soc.*, **135**, 7909 (2013).
23. O. Yamamoto, Y. Takeda, R. Kanno and M. Noda, *Solid State Ionics*, **22**, 241 (1987).
24. N. Q. Minh, *J. Am. Ceram. Soc.*, **76**, 563 (1993).
25. S. P. S. Badwal, R. Deller, K. Foger, Y. Ramprakash and J. P. Zhang, *Solid State Ionics*, **99**, 297 (1997).
26. S. P. Jiang, *Solid State Ionics*, **146**, 1 (2002).
27. Y. Matsuzaki and I. Yasuda, *Solid State Ionics*, **132**, 271 (2000).
28. Y. Matsuzaki and I. Yasuda, *J. Electrochem. Soc.*, **148**, A126 (2001).
29. S. P. Jiang, J. P. Zhang and X. G. Zheng, *J. European Ceram. Soc.*, **22**, 361 (2002).
30. J. Nielsen and M. Mogensen, *Solid State Ionics*, **189**, 74 (2011).
31. R. R. Liu, S. H. Kim, S. Taniguchi, T. Oshima, Y. Shiratori, K. Ito and K. Sasaki, *J. Power Sources*, **196**, 7090 (2011).
32. S. H. Kim, K. B. Shim, C. S. Kim, J. T. Chou, T. Oshima, Y. Shiratori, K. Ito and K. Sasaki, *J. Fuel Cell Sci. Technol.*, **7**, 6 (2010).

33. T. A. Jin and K. Lu, *J. Power Sources*, **197**, 20 (2012).
34. C. Pellegrinelli, Y.-L. Huang, J. A. Taillon, L. G. Salamanca-Riba and E. D. Wachsman, *ECS Trans.*, **64**, 17 (2014).
35. C. Knöfel, M. Chen and M. Mogensen, *Fuel Cells*, **11**, 669 (2011).
36. V. Sharma, M. K. Mahapatra, S. Krishnan, Z. Thatcher, B. D. Huey, P. Singh and R. Ramprasad, *J. Mater. Chem. A*, **4**, 5605 (2016).
37. A. Hauch, S. H. Jensen, J. B. Bilde-Sorensen and M. Mogensen, *J. Electrochem. Soc.*, **154**, A619 (2007).
38. E. J. Opila, D. L. Myers, N. S. Jacobson, I. M. B. Nielsen, D. F. Johnson, J. K. Olminky and M. D. Allendorf, *J. Phys. Chem. A*, **111**, 1971 (2007).
39. A. Hagen, M. Chen, K. Neufeld and Y.-L. Liu, *ECS Transactions*, **25**, 439 (2009).
40. J. Nielsen, A. Hagen and Y. L. Liu, *Solid State Ionics*, **181**, 517 (2010).
41. Z. Zhao, L. Liu, X. Zhang, W. Wu, B. Tu, D. Ou and M. Cheng, *J. Power Sources*, **222**, 542 (2013).
42. B. Hu, M. K. Mahapatra, M. Keane, H. Zhang and P. Singh, *J. Power Sources*, **268**, 404 (2014).
43. S. Darvish, M. Asadikiya, B. Hu, P. Singh and Y. Zhong, *Int. J. Hydrogen Energy*, **41**, 10239 (2016).
44. B. X. Hu, M. K. Mahapatra and P. Singh, *J. Ceram. Soc. Jpn.*, **123**, 199 (2015).
45. S. Jiang and J. Love, *Solid State Ionics*, **138**, 183 (2001).
46. K. Katsiev, B. Yildiz, K. Balasubramaniam and P. A. Salvador, *Appl. Phys. Lett.*, **95**, 092106 (2009).
47. A. A. Vance and S. McIntosh, *J. Electrochem. Soc.*, **155**, B1 (2007).
48. A.-K. Huber, M. Falk, M. Rohnke, B. Luerssen, M. Amati, L. Gregoratti, D. Hesse and J. Janek, *J. Catal.*, **294**, 79 (2012).
49. T. T. Fister, D. D. Fong, J. A. Eastman, P. M. Baldo, M. J. Highland, P. H. Fuoss, K. R. Balasubramaniam, J. C. Meador and P. A. Salvador, *Appl. Phys. Lett.*, **93**, 151904 (2008).
50. S. B. Adler, *Chem. Rev.*, **104**, 4791 (2004).
51. Y. J. Leng, S. H. Chan, K. A. Khor and S. P. Jiang, *J. Appl. Electrochem.*, **34**, 409 (2004).
52. Y.-K. Lee, J.-Y. Kim, Y.-K. Lee, I. Kim, H.-S. Moon, J.-W. Park, C. P. Jacobson and S. J. Visco, *J. Power Sources*, **115**, 219 (2003).
53. S. Koch, M. Mogensen, P. V. Hendriksen, N. Dekker and B. Rietveld, *Fuel Cells*, **6**, 117 (2006).
54. F. H. van Heuveln and H. J. M. Bouwmeester, *J. Electrochem. Soc.*, **144**, 134 (1997).
55. Y. Jiang, S. Z. Wang, Y. H. Zhang, J. W. Yan and W. Z. Li, *J. Electrochem. Soc.*, **145**, 373 (1998).
56. Y. Jun, H. Muroyama, T. Matsui and K. Eguchi, in *Solid Oxide Fuel Cells 11*, S. C. Singhal and H. Yokokawa Editors, p. 2349, Electrochemical Soc Inc, Pennington (2009).
57. J. Yang, H. Muroyama, T. Matsui and K. Eguchi, *Inter. J. Hydrogen Energy*, **35**, 10505 (2010).
58. X. J. Chen, K. A. Khor and S. H. Chan, *Solid State Ionics*, **167**, 379 (2004).
59. J. D. Kim, G. D. Kim, J. W. Moon, Y. I. Park, W. H. Lee, K. Kobayashi, M. Nagai and C. E. Kim, *Solid State Ionics*, **143**, 379 (2001).
60. S. P. Jiang, *J. Solid State Electrochem.*, **11**, 93 (2007).
61. H. Y. Lee, W. S. Cho, S. M. Oh, H. D. Wiemhöfer and W. Göpel, *J. Electrochem. soc.*, **142**, 2659 (1995).
62. E. Siebert, A. Hammouche and M. Kleitz, *Electrochim. Acta*, **40**, 1741 (1995).
63. K. Yasumoto, N. Mori, J. Mizusaki, H. Tagawa and M. Dokiya, *J. Electrochem. Soc.*, **148**, A105 (2001).
64. M. Backhaus-Ricoult, K. Adib, T. S. Clair, B. Luerssen, L. Gregoratti and A. Barinov, *Solid State Ionics*, **179**, 891 (2008).
65. W. Wang and S. P. Jiang, *J. Solid State Electrochem.*, **8**, 914 (2004).
66. S. P. Jiang and W. Wang, *Electrochem. Solid-State Lett.*, **8**, A115 (2005).
67. M. A. Haider and S. McIntosh, *J. Electrochem. Soc.*, **156**, B1369 (2009).
68. A. A. Vance and S. McIntosh, *J. Electrochem. Soc.*, **155**, B1 (2008).

69. S. P. Jiang and J. G. Love, *Solid State Ionics*, **138**, 183 (2001).
70. M. Backhaus-Ricoult, K. Adib, T. St.Clair, B. Luerssen, L. Gregoratti and A. Barinov, *Solid State Ionics*, **179**, 891 (2008).
71. A. Mitterdorfer and L. J. Gauckler, *Solid State Ionics*, **111**, 185 (1998).
72. A. Weber, R. Männer, B. Jobst, M. Schiele, H. Cerva, R. Waser and E. Ivers-Tiffée, *High Temp. Electrochem.: Ceram. Met.*, 473 (1996).
73. E. Ivers-Tiffée, A. Weber, K. Schmid and V. Krebs, *Solid State Ionics*, **174**, 223 (2004).
74. A. K. Huber, M. Falk, M. Rohnke, B. Luerssen, M. Amati, L. Gregoratti, D. Hesse and J. Janek, *J. Catal.*, **294**, 79 (2012).
75. M. L. Traulsen, C. Chatzichristodoulou, K. V. Hansen, L. T. Kuhn, P. Holtappels and M. B. Mogensen, *ECS Transactions*, **66**, 3 (2015).
76. J. S. Hardy, J. W. Templeton and J. W. Stevenson, in *Advances in Solid Oxide Fuel Cells VIII*, p. 71, John Wiley & Sons, Inc. (2012).
77. H. B. Mann and D. R. Whitney, *Ann. Math. Stat.*, **18** (1947).
78. S. Kotz, N. L. Johnson, *Breakthroughs in Statistics*, (1992).
79. Y. L. Liu, A. Hagen, R. Barfod, M. Chen, H.-J. Wang, F. W. Poulsen and P. V. Hendriksen, *Solid State Ionics*, **180**, 1298 (2009).
80. F. Zheng and L. R. Pederson, *J. Electrochem. Soc.*, **146**, 2810 (1999).
81. S. Jiang, J. Love, J. Zhang, M. Hoang, Y. Ramprakash, A. Hughes and S. Badwal, *Solid State Ionics*, **121**, 1 (1999).
82. N. Li, *Doctoral Dissertations*, **320** (2014).
83. R. Moriche Tirado, D. Marrero López, F. J. Gotor Martínez and M. J. Sayagués de Vega, *J. Power Sources*, 252, 43-50. (2014).
84. R. Millini, M. Gagliardi and G. Piro, *J. mater. Sci.*, **29**, 4065 (1994).
85. A. Hammouche, E. Siebert and A. Hammou, *Mater. Res. Bull.*, **24**, 367 (1989).
86. J. H. Lee, H. Moon, H. W. Lee, J. Kim, J. D. Kim, K. H. Yoon, *Solid State Ionics*, **148**, 15 (2002).
87. RCore, T. E. A. M., R Foundation for Statistical Computing, Vienna, Austria, (2016).

Figures with captions:

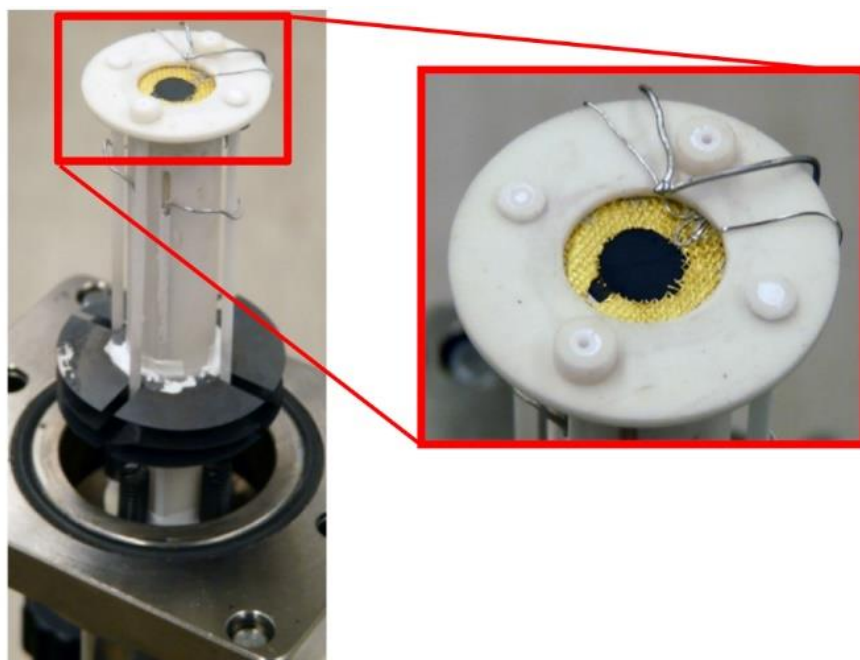


Figure 1. Top of the *in-operando* XRD test fixture with cell attached.

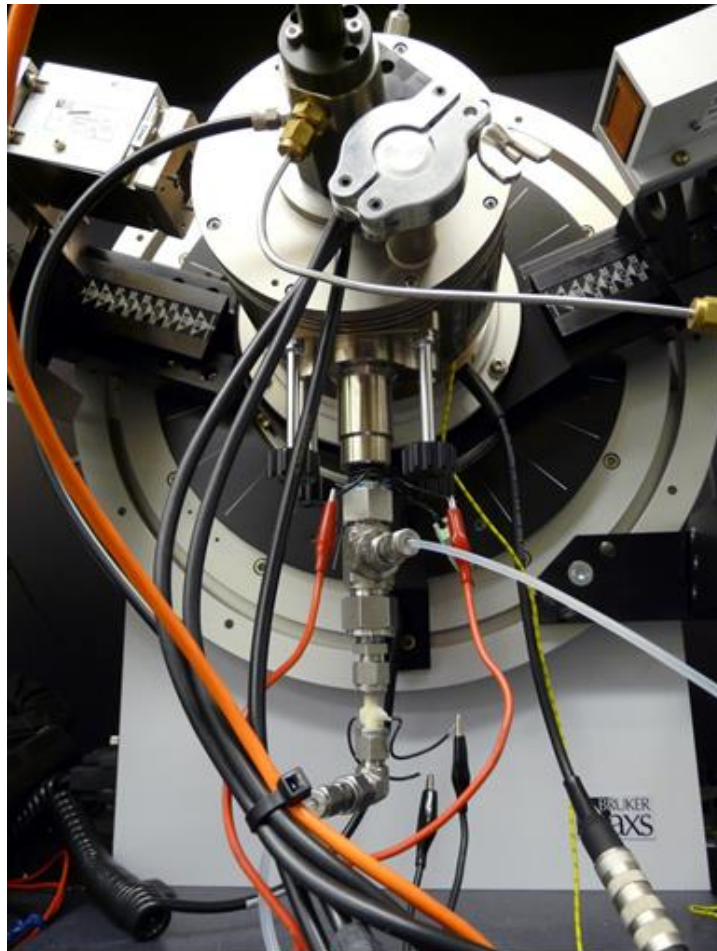


Figure 2. The test fixture inserted into the Anton Paar HTK 1200 heating chamber.

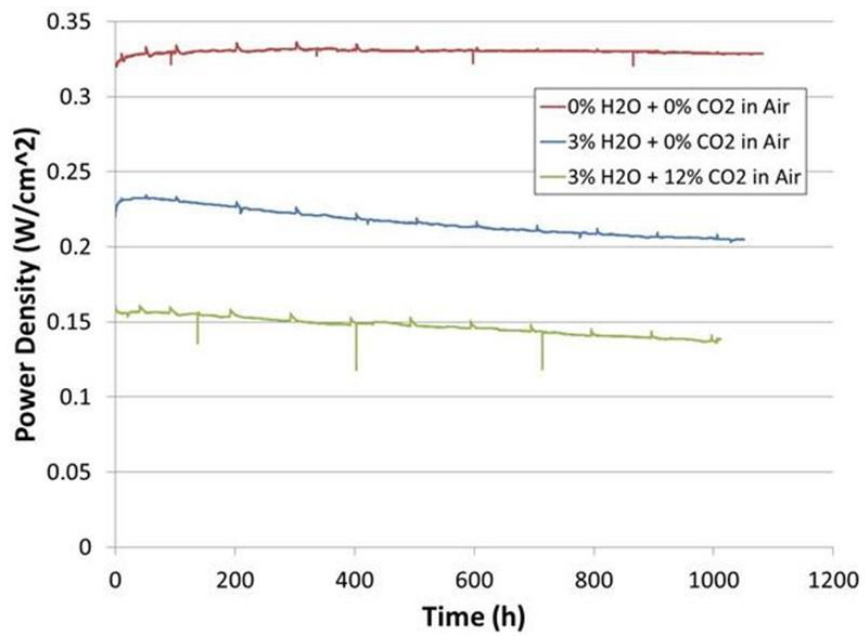


Figure 3. Power density as a function of time for cells operated in the *in-operando* XRD test stand at ~ 0.8 V.

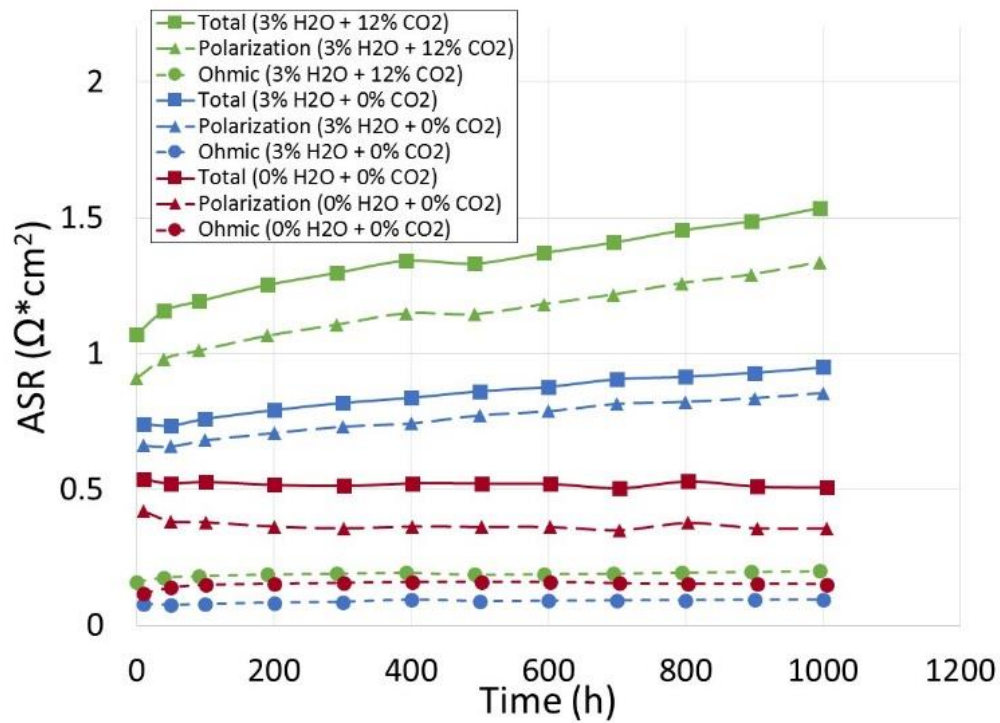


Figure 4. Ohmic (a) and polarization (b) contributions to total (c) ASR from impedance analysis of cells during in-operando XRD.

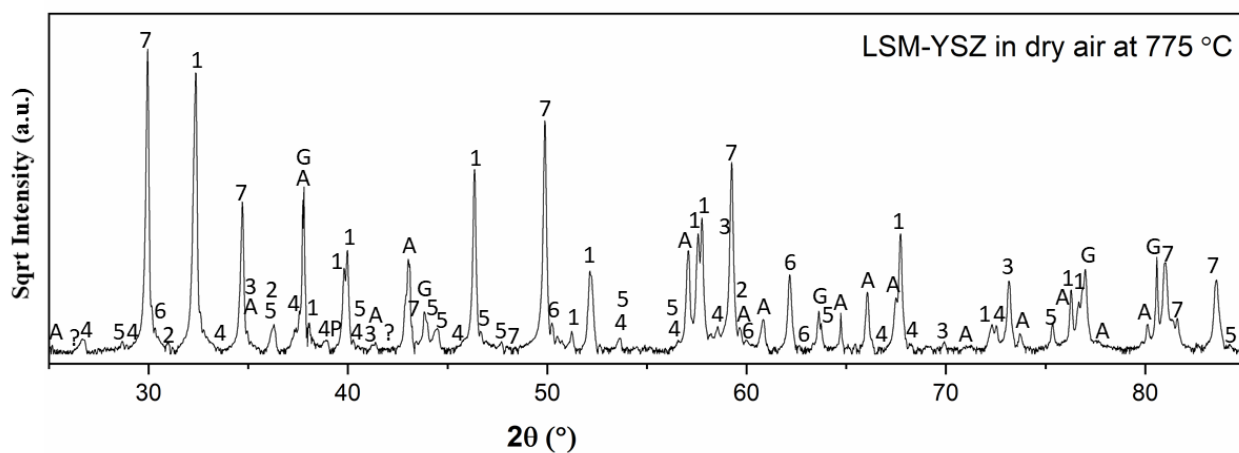


Figure 5. XRD pattern summation of all patterns collected from the LSM-YSZ cathode tested in clean dry air at 775°C under constant current during 1080 hours of testing. Square foot of peak intensities were presented to magnify minor secondary phases. Peaks labels correspond to the following identified phases: 1 = LSM; 2 = Mn_3O_4 ; 3 = MnO ; 4 = $\text{La}_2\text{Zr}_2\text{O}_7$; 5 = La_2O_3 ; 6 = Tet-YSZ; 7 = YSZ; G = Gold; P = Pt; A = Alumina; ? = unidentified.

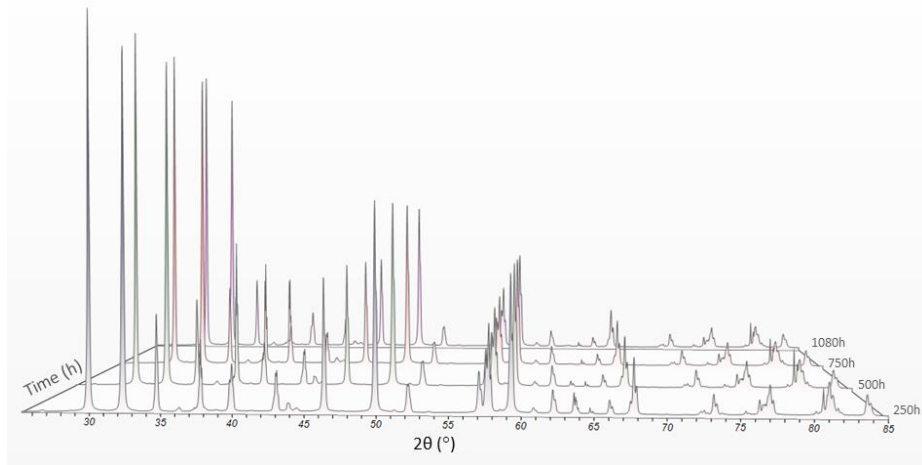


Figure 6. Time dependant phase evolution of the LSM-YSZ cathode operated in clean dry air at 775 °C at ~0.8 V obtained by summed-up XRD pattern of every 250 individual patterns

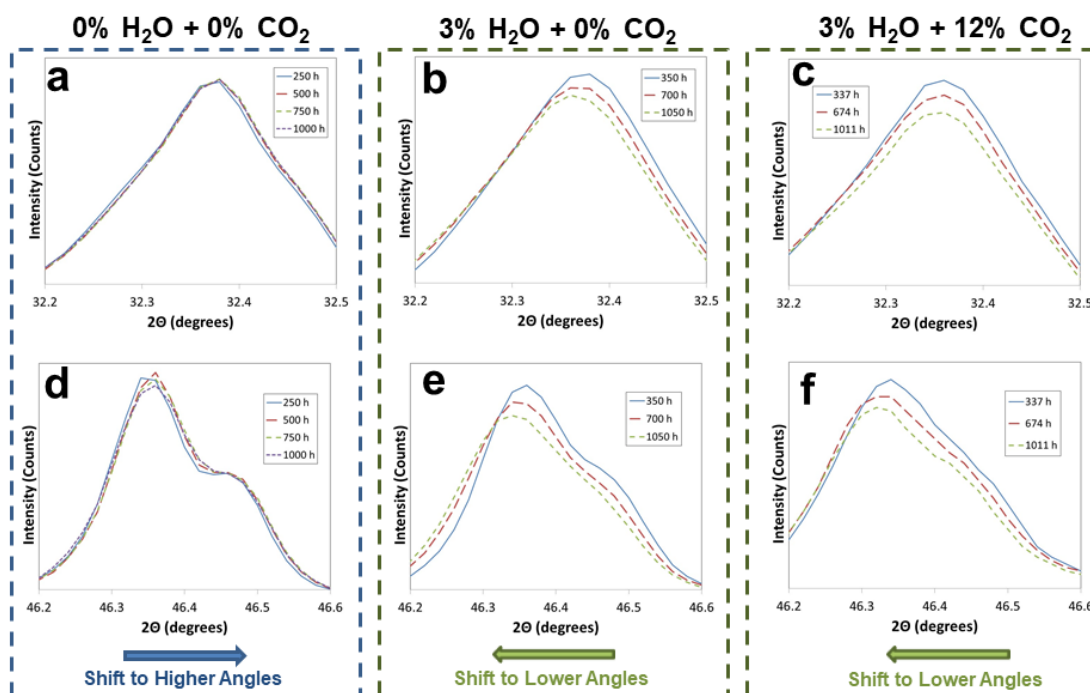


Figure 7. Gradual changes of the major peaks of LSM in integrated *in-operando* XRD patterns of LSM-YSZ cathodes operated at $\sim 0.8\text{V}$ and 775°C in (a, d) dry air, (b, e) humid air, and (c, f) humid air with added CO_2 .

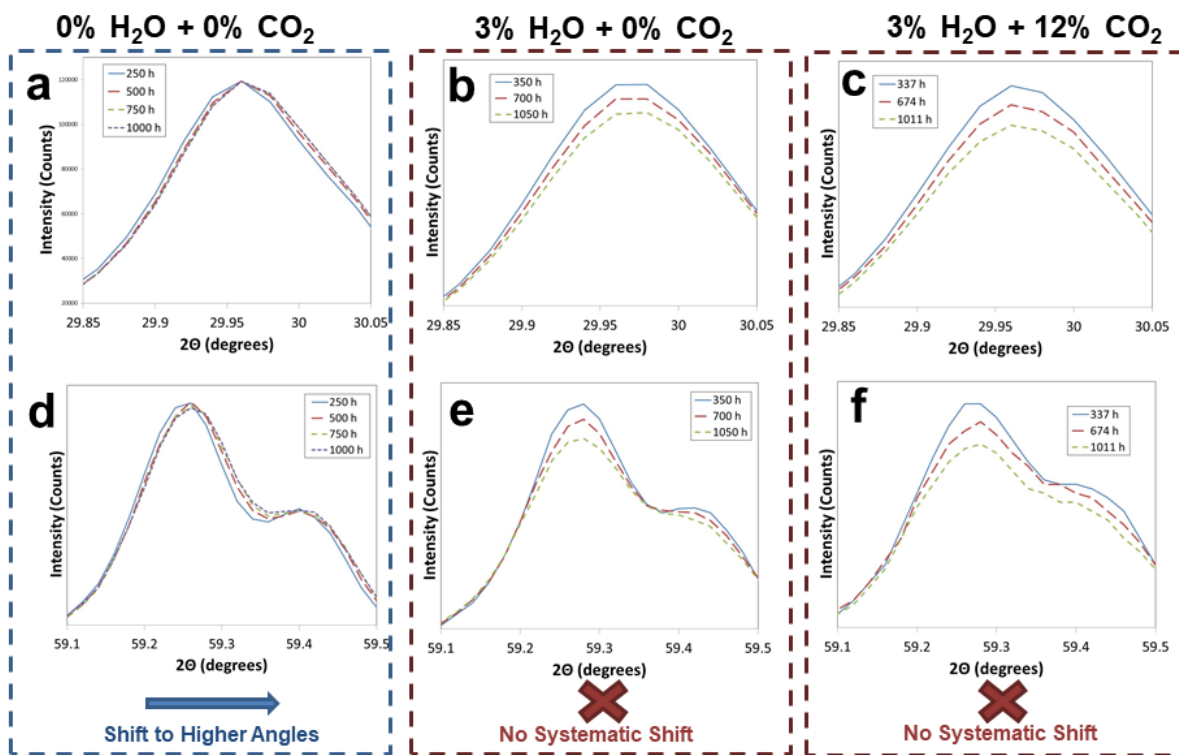
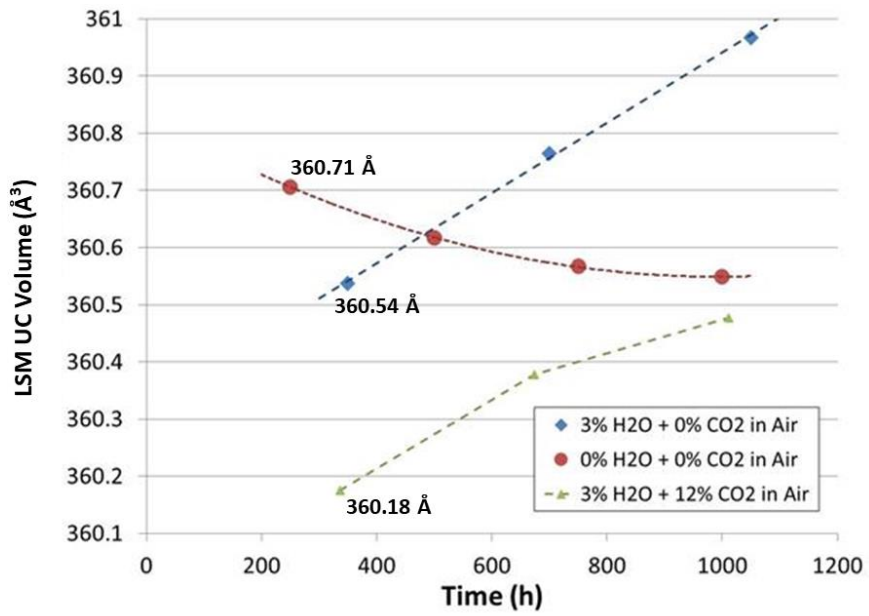


Figure 8. Peak shifts of the major peaks of YSZ in integrated *in-operando* XRD patterns of LSM-YSZ cathodes operated at $\sim 0.8\text{V}$ and $775\text{ }^\circ\text{C}$ in (a, d) dry air, (b, e) humid air, and (c, f) humid air with added CO_2 .



1

Figure 9. LSM unit cell volume obtained by integrated *in-operando* XRD patterns of LSM-YSZ cathodes operated at $\sim 0.8\text{V}$ and $775\text{ }^\circ\text{C}$ in varying cathode air compositions.

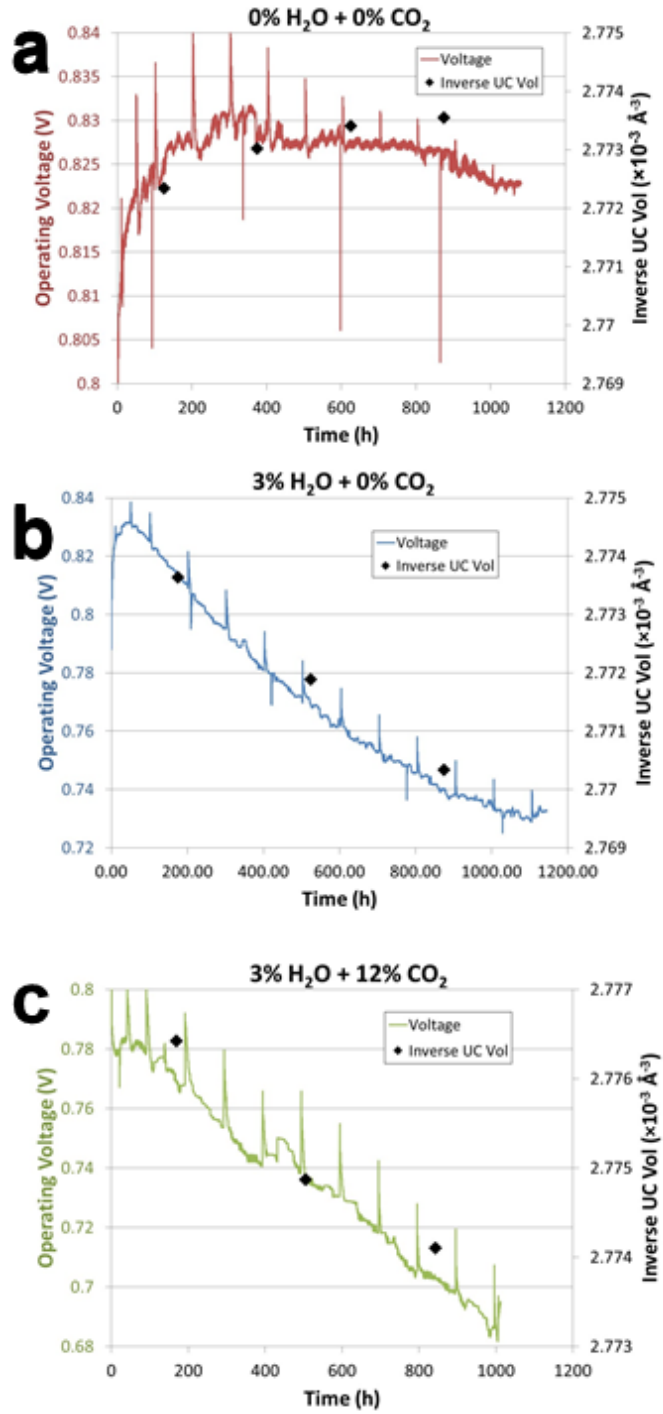


Figure 10. A comparison between the operating voltage and inverse unit cell volume of LSM of the cells tested at constant current and 775 °C in (a) dry air, (b) humid air, and (c) humid air with added CO₂.

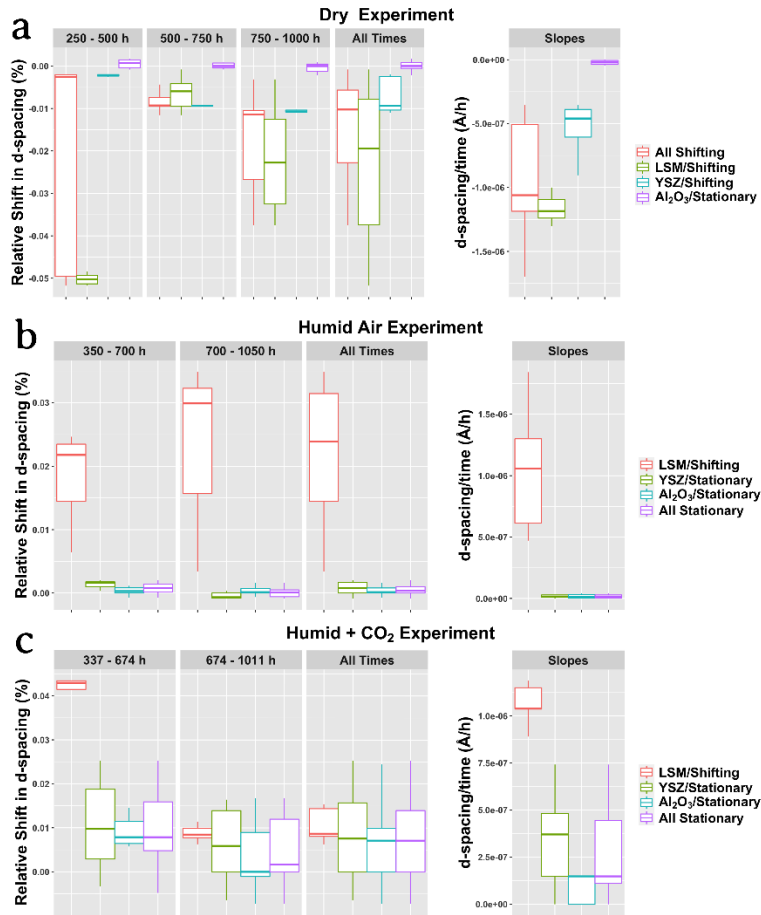


Figure 11. Measurements of HT-XRD peak movements, including the relative peak shifts measured for separate time intervals and for a collective of all intervals and the slopes from the linear fit approximation to time dependent data with respect to each individual phase, from experiments conducted at $\sim 0.8V$ and $775^\circ C$ in (a) dry air, (b) humid air, and (c) humid air with added CO_2 . Outlier point from the LSM group that has a large positive value from the 250-700h period is not shown, and 1 outlier point from the LSM group that has a large negative value from the 700-1050h period is not shown. This means that those two points are also hidden from the "All Times" data set.

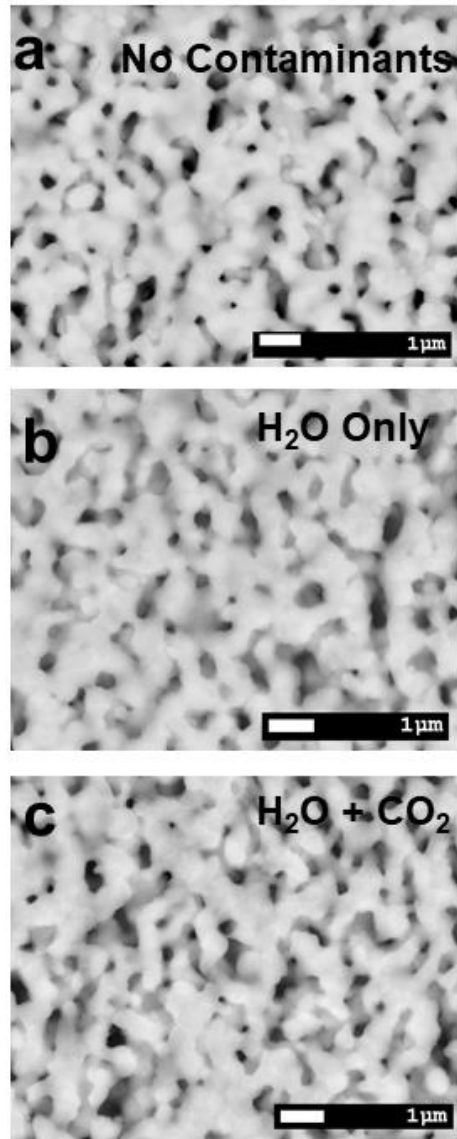


Figure 12. Field emission SEM micrographs of cathode surfaces of the cells tested at $\sim 0.8\text{V}$ and $775\text{ }^\circ\text{C}$ in (a) dry air, (b) humid air, and (c) humid air with added CO_2 .

Tables with captions:

Table 1. Concentrations (wt%) of phases identified by *in-operando* XRD of LSM-YSZ cathodes operating under various cathode air compositions at constant current

	0% H ₂ O + 0% CO ₂	3% H ₂ O + 0% CO ₂	3% H ₂ O + 12% CO ₂
LSM	45.7 +/- 1.1	46.4 +/- 1.1	45.2 +/- 2.2
YSZ	43.3 +/- 1.2	45.0 +/- 1.0	45.1 +/- 2.4
Tet-YSZ	0.6 +/- 0.1	1.0 +/- 0.5	1.1 +/- 0.8
Mn ₃ O ₄	3.0 +/- 0.2	2.3 +/- 0.2	2.1 +/- 0.4
MnO	2.1 +/- 0.2	1.1 +/- 0.1	6.0 +/- 0.9
La ₂ O ₃	1.8 +/- 0.2	1.9 +/- 0.2	0.3 +/- 0.1
La ₂ Zr ₂ O ₇	<0.1	<0.1	0.1 +/- 0.1

Table 2. Rate of Sr loss that correlates to the expansion rate of LSM unit cell lattice

Å ³ /h	Å ³ /x in La _{1-x} Sr _x MnO ₃		- x/h
	min	max	
0.0006	20.540*	24.036*	3×10 ⁻⁵

* denotes the effect of Sr loss on unit cell volume are referenced from (83-85)

Table 3. Results of statistical analysis of time dependent shift, time independent shift and time dependent slope of *in-operando* HT- XRD peaks tested at 775 °C at ~0.8V.

Dry Experiment												
Shifting phases	Stationary phases	Tests	Comparison between different time period						Time Independent % shift		Time dependent slope	
			250h-500h		500h-750h		750h-1000h		p-values	Accept	p-values	Accept
LSM; YSZ	Al ₂ O ₃		p-values	Accept	p-values	Accept	p-values	Accept	p-values	Accept	p-values	Accept
		Al ₂ O ₃ =0?	1.24×10 ⁻¹	=	4.47×10 ⁻¹	=	4.47×10 ⁻¹	=	2.94×10 ⁻¹	=	2.75×10 ⁻¹	=
		Stationary =shifting?	8.50×10 ⁻⁶	≠	1.08×10 ⁻¹	≠	8.42×10 ⁻⁶	≠	1.06×10 ⁻⁹	≠	3.10×10 ⁻⁸	≠
		LSM vs YSZ	7.56×10 ⁻⁵	LSM<YSZ	3.49×10 ⁻³	LSM<YSZ	1.57×10 ⁻²	LSM<YSZ	5.34×10 ⁻³	LSM<YSZ	3.13×10 ⁻⁶	LSM<YSZ
		LSM vs Al ₂ O ₃	5.10×10 ⁻⁷	LSM<Al ₂ O ₃	5.12×10 ⁻¹	LSM<=YSZ	2.32×10 ⁻⁵	LSM<Al ₂ O ₃	1.03×10 ⁻⁶	LSM<Al ₂ O ₃	5.10×10 ⁻⁷	LSM<Al ₂ O ₃
		YSZ vs Al ₂ O ₃	2.23×10 ⁻⁴	YSZ<Al ₂ O ₃	2.15×10 ⁻⁴	YSZ<Al ₂ O ₃	2.15×10 ⁻⁴	YSZ<Al ₂ O ₃	2.90×10 ⁻¹⁰	YSZ<Al ₂ O ₃	2.29×10 ⁻⁵	YSZ<Al ₂ O ₃
		Shifting vs Stationary	4.25×10 ⁻⁶	Shifting<Stationary	5.41×10 ⁻²	Shifting>=Stationary	4.21×10 ⁻⁶	Shifting<Stationary	5.32×10 ⁻¹⁰	Shifting<Stationary	1.55×10 ⁻⁸	Shifting<Stationary
Humid Air Experiment												
Shifting phases	Stationary phases	Tests	Comparison between different time period				Time Independent % shift		Time dependent slope			
			350h-700h		700h-1050h		p-values	Accept	p-values	Accept		
LSM	YSZ; Al ₂ O ₃		p-values	Accept	p-values	Accept	Accept	p-values	Accept	p-values	Accept	
		Al ₂ O ₃ =0?	1.24×10 ⁻¹	=	4.77×10 ⁻¹	=	1.17×10 ⁻¹	=	2.32×10 ⁻¹	=		
		Stationary =shifting?	1.86×10 ⁻⁶	≠	4.42×10 ⁻⁵	≠	2.50×10 ⁻¹⁰	≠	1.86×10 ⁻⁶	≠		
		LSM vs YSZ	7.56×10 ⁻⁵	LSM>YSZ	5.92×10 ⁻⁴	LSM>YSZ	2.07×10 ⁻⁷	LSM>YSZ	7.56×10 ⁻⁵	LSM>YSZ		
		LSM vs Al ₂ O ₃	2.35×10 ⁻⁵	LSM>Al ₂ O ₃	2.46×10 ⁻⁴	LSM>Al ₂ O ₃	2.86×10 ⁻⁸	LSM>Al ₂ O ₃	5.10×10 ⁻⁷	LSM>Al ₂ O ₃		
		YSZ vs Al ₂ O ₃	3.11×10 ⁻³	YSZ>Al ₂ O ₃	1.04×10 ⁻²	YSZ<Al ₂ O ₃	4.56×10 ⁻¹	YSZ<=Al ₂ O ₃	4.12×10 ⁻¹	YSZ<=Al ₂ O ₃		
		Shifting vs Stationary	9.31×10 ⁻⁷	Shifting>Stationary	2.21×10 ⁻⁵	Shifting>Stationary	1.25×10 ⁻¹⁰	Shifting>Stationary	9.31×10 ⁻⁷	Shifting>Stationary		
Humid+CO ₂ Experiment												
Shifting phases	Stationary phases	Tests	Comparison between different time period				Time Independent % shift		Time dependent slope			
			337h-674h		674h-101h		p-values	Accept	p-values	Accept		
LSM	YSZ; Al ₂ O ₃		p-values	Accept	p-values	Accept	p-values	Accept	p-values	Accept		
		Al ₂ O ₃ =0?	6.25×10 ⁻¹	=	8.00×10 ⁻¹	=	5.38×10 ⁻¹	=	6.9510 ⁻¹	=		
		Stationary =shifting?	1.86×10 ⁻⁶	≠	8.33×10 ⁻²	≠	8.16×10 ⁻⁶	≠	1.84×10 ⁻⁶	≠		
		LSM vs YSZ	7.56×10 ⁻⁵	LSM>YSZ	2.81×10 ⁻¹	LSM>YSZ	1.64×10 ⁻³	LSM>YSZ	7.40×10 ⁻⁵	LSM>YSZ		
		LSM vs Al ₂ O ₃	2.33×10 ⁻⁵	LSM>Al ₂ O ₃	1.62×10 ⁻²	LSM>Al ₂ O ₃	6.48×10 ⁻⁶	LSM>Al ₂ O ₃	2.30×10 ⁻⁵	LSM>Al ₂ O ₃		
		YSZ vs Al ₂ O ₃	1.37×10 ⁻¹	YSZ>Al ₂ O ₃	8.20×10 ⁻²	YSZ<Al ₂ O ₃	2.78×10 ⁻²	YSZ>Al ₂ O ₃	1.33×10 ⁻²	YSZ>Al ₂ O ₃		
		Shifting vs Stationary	9.31×10 ⁻⁷	Shifting>Stationary	4.17×10 ⁻²	Shifting>Stationary	4.08×10 ⁻⁶	Shifting>Stationary	9.21×10 ⁻⁷	Shifting>Stationary		